NUMERICAL ANALYSIS OF HUB AND FUSELAGE DRAG BREAKDOWN OF A HELICOPTER CONFIGURATION

T. Renaud[*]*, A. Le Pape*[*]*, S. Péron*[**]

[*] *ONERA, The French Aerospace Lab, F-92190, Meudon, France*
Email address: thomas.renaud@onera.fr
Phone number: (33) 1 46 73 42 40
Fax number: (33) 1 46 73 41 46

[**] *ONERA, The French Aerospace Lab, F-92322 Châtillon, France*

Abstract

Compared to fixed wing aircraft, the helicopter is still a challenging configuration in terms of drag evaluation and understanding. In order to reduce and optimize the drag, the interactions between all components of fuselage and rotor head have to be analyzed. Thanks to the computational resources increase, the CFD becomes an efficient tool, complementary to the wind tunnel testing, in order to investigate different geometries and flow conditions. In the frame of the JTI CleanSky European project, the work presented in this paper is a preliminary task before the optimization and the drag reduction. It deals with the drag prediction of the fuselage and its main rotor head by CFD. The approach used here relies on a partitioning of the computational domain into near-body structured grids and off-body Cartesian grids, based on the Chimera method. The current work includes analysis of solutions for the isolated fuselage, the isolated rotor head and the complete configuration.

1. INTRODUCTION

This study has been performed in the frame of the JTI CleanSky European project (2008-2015), where the Green Rotorcraft (GRC) deals with the environmental impact of helicopters. A subtask of this project (GRC2) focuses in particular on the improvement of the helicopter drag prediction and reduction thanks to the CFD tool and aims at reducing the fuel consumption. Actually, the drag of a helicopter is in general greater than a fixed wing aircraft, due to the numerous components added to the fuselage (blades, rotor hub, skids, empennages…). In particular, it is now well known that the hub may contribute up to 30% of the total drag, or even more for high speed rotorcrafts.

Therefore, a significant amount of research efforts have been dedicated to the analysis and reduction of the helicopter hub drag. The vast majority of the research relied on wind tunnel measurements. In 1976, Sheehy *et al.*[1] analyzed different test data to identify the main parameters affecting the helicopter hub drag such as the hub frontal area or the pylon shape and performed the development of a hub drag prediction method. At the end of the 80's, Graham *et al.*[2] studied particularly the interference of the hub fairing with the pylon with the objective of drag reduction. In 1985, a wind tunnel test was conducted to investigate rotor hub drag reduction by the use of fairings [3] with analysis of the effects on rotor hub drag of various parameters: angle of attack, Mach number, hub rotation and hub fairing shape.

Generally, in experimental hub drag analysis, the interactions between only few elements (hub, fairings and pylon) are studied. A helicopter rotor head is more complex and different parts of its geometry can influence the wake and the drag evaluation. Thanks to the growth of computational resources, CFD has become an efficient way to investigate configurations or complex problems that wind tunnel tests cannot answer to. The review of literature about the rotor hub drag evaluation by CFD leads to a few and recent papers: it reveals that this topic has been for many years only studied in an experimental approach. Thanks to the maturity of CFD codes and the increasing computing performances, the authors are now able to deal with this problem. Nevertheless, the estimation of the rotor head drag is still challenging due to the complexity of geometries and the mutual interactions between rotating and non-rotating elements.

In [4], Borie *et al.* performed the CFD simulation of a complete rotor head and the drag decomposition by elements in a structured overset grid approach. The process is to compute different configurations by adding, step by step,

each representative element of the rotor hub (mast, cap, blade sleeves, lead-lag dampers, blade roots), above a fuselage. In order to simplify the mesh generation of the complete configuration using structured grids and in order to add elements without remeshing, the overset grid approach has been used. A high level of realistic geometry can be reached by using unstructured grids, as done by Le Chuiton *et al*. [5], Bridgeman *et al*. [6] or recently by Dombroski *et al.* [7]. This work of drag evaluation and analysis is a first step before studying optimization for drag reduction.

In this paper, the work achieved at ONERA on the numerical analysis of hub and fuselage drag is presented. To investigate the effect of geometric elements by numerous CFD computations, it is important to rely on an efficient mesh strategy. Here, the computational domain is divided into near-body regions and off-body regions, where near-body regions are meshed with structured grids describing the different geometrical elements, and off-body regions are described by a set of adaptive Cartesian grids in an overset grid framework. Each element is meshed separately, and an overset grid assembly is performed between overlapping near-body grids. The first part of the paper describes the numerical methods and the overset grid assembly process. Then, the drag breakdown of an isolated fuselage is presented. Finally, the interactions between the fuselage and the rotor head are analysed through the drag evaluation. A wind tunnel test is planned in 2014 in the JTI-GRC2 project, so no experimental data can be compared with the numerical solutions in this paper.

2. NUMERICAL METHODS

2.1. Description of the flow solver

The simulations have been performed using elsA structured CFD solver [8], developed at ONERA. The 3D compressible RANS equations are solved by a Finite-Volume cell-centred approach for both off-body Cartesian and near-body curvilinear grids.

All the simulations of the present paper have been run using a 2nd-order Jameson scheme. The time integration is ensured by a 2nd-order backward Euler scheme and an implicit LU-SSOR phase. The turbulence model is a k-ω Kok model with the addition of the Menter SST correction and a Zheng limiter. First, steady-state simulations are performed until convergence, and then are used as initial state of unsteady computations, taking into account the motion of the components. A Gear subiteration method is applied to reach 2nd-order time accuracy with a final time step corresponding to an azimuthal increment of $\Delta\Psi=1°$. 7 to 8 rotor revolutions are run to ensure a good convergence of the loads.

2.2. Description of the mesh

The wind tunnel model (scale 1:3.881) is based on an Agusta helicopter model, composed by a fuselage and a main rotor head. The fuselage looks like a NH90 helicopter and was used in a previous European program, called GoAhead (2005-2009) [9].

In order to avoid time consumption in the meshing process, the initial geometry of the main rotor head has been simplified. The main parts of the rotor head, in terms of drag contribution (drag breakdown estimation coming from literature and a previous study), have been retained, as shown in Figure 1.

The scissors are removed, as they rotate into the fuselage cavity and should not contribute to the global drag at a significant level. The rotor stubs (grey) are cut at root whereas the blade attachment (green) geometry is closed. The dampers (orange) and the rods (red) are not attached to the rest of the configuration, for the sake of mesh simplification. The hub cap (beanie) and the mast constitute a single part, named “rotor mast” (purple).

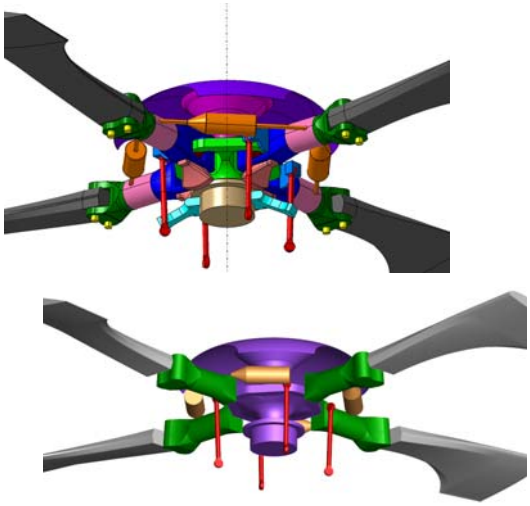

Figure 1 - Comparison between the initial and the simplified geometries of the rotor head

Each part of the configuration has been meshed separately in an overset grid approach, simplifying the mesh generation process. Each element is meshed by a set of abutting curvilinear grids extending a short distance into the domain. The use of overset grids enables to add or remove a feature on the configuration easily. Table 1

presents the size (in Million points) of each component. Figure 2 and Figure 3 show the extension of the near-body grid and the surface mesh for the fuselage and each part of the rotor head.

Table 1 - Mesh size of near-body grids

Fuselage	8M
Rotor mast	12.6M
Damper	0.25M
Blade attachment	1.6M
Blade stub	0.94M
Rod	1.1M

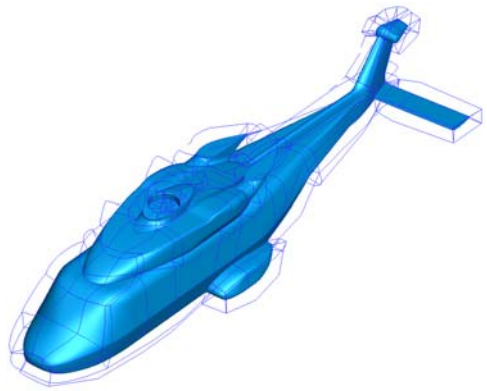

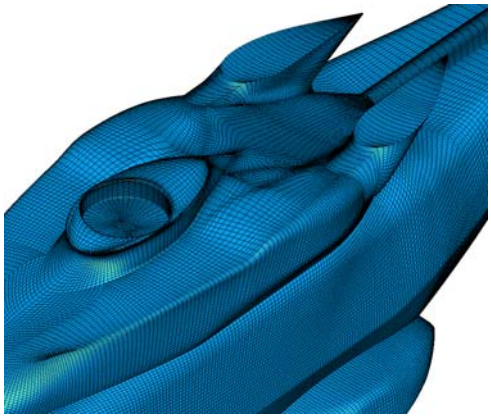

Figure 2 - Near-body grid of the fuselage

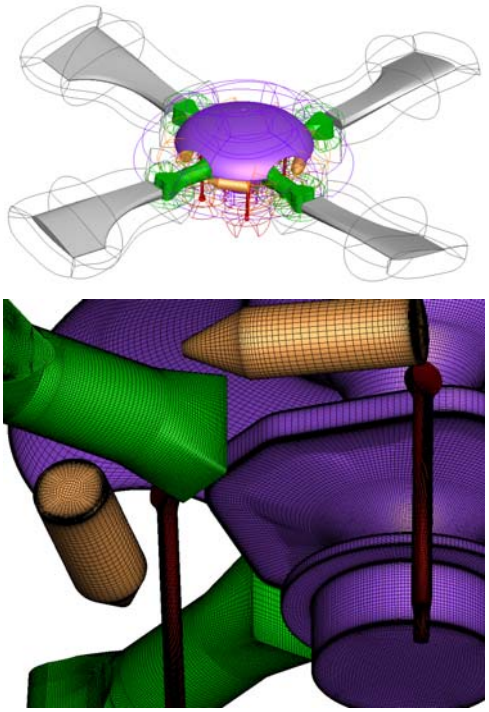

Figure 3 - Near-body grids of the simplified rotor head

2.3. Automatic generation of off-body adaptive Cartesian grids and Chimera assembly

In order to improve the automation of the mesh generation process, the key-concept of near-body/off-body mesh partitioning, introduced by Meakin [11] is used here. In order to take into account the large scale discrepancies in terms of mesh resolution around each component, the octree-based adaptive Cartesian off-body mesh generation developed by Péron and Benoit is used [12]. The method consists in building automatically an octree structure starting from a set of surfaces and a set of spacings required in the vicinity of each surface. Then, the off-body Cartesian mesh derives from the octree structure, assuming that each octree leaf describes an uniform Cartesian grid. Each input surface is defined here by the external borders of the near-body mesh of a component. The Cartesian mesh can be derived into a hierarchical or a patched-grid fashion, which is performed here. The spacing required for Cartesian grids in the vicinity of each near-body mesh is defined as the average value of the cell size at its external borders, such that interpolation errors during Chimera transfers between near-body and off-body grids are kept as small as possible. Figure 4 displays views of the Cartesian off-body mesh in the median plane Y=0 for the three configurations: isolated fuselage, isolated rotor head and complete configuration.

To simplify the mesh generation process, the rods have been removed in the complete configuration: as it will be shown with the numerical results, the drag contribution of the rods is weak. For all configurations, the minimum cell size around the fuselage or around the rotor head (half the one around the fuselage) is kept identical. Thus, the generated Cartesian mesh contains about 42.5M points for the isolated fuselage configuration, 33.6M points for the isolated rotor head configuration and 26.8 M points for the complete configuration (the extension of the finest Cartesian grid is smaller for this last configuration than the two others).

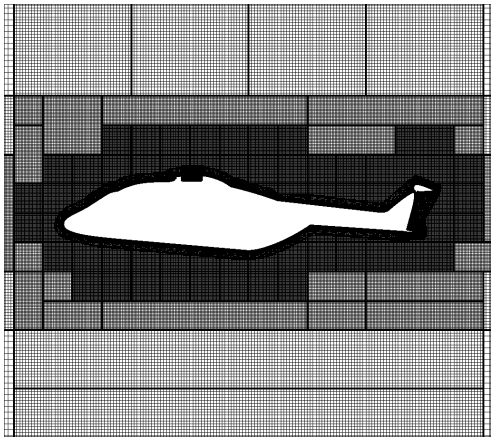

(a)

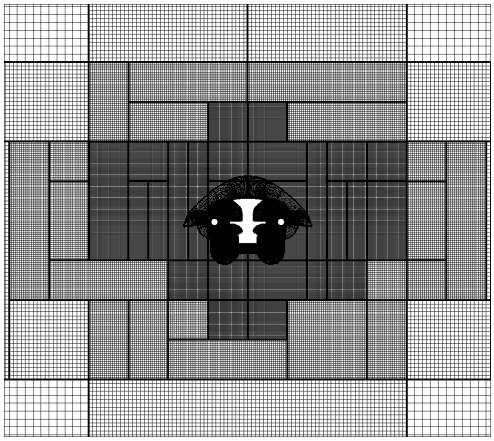

(b)

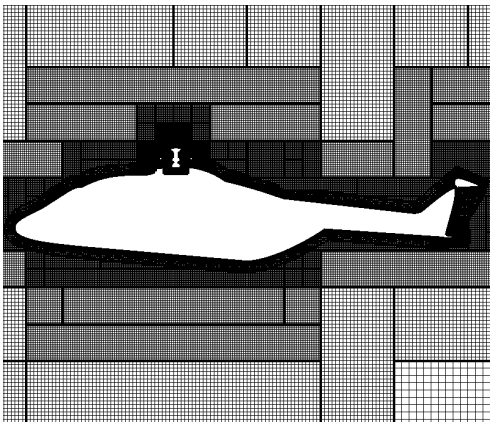

(c)

Figure 4 - Views of the Cartesian background grid for the isolated fuselage (a), the isolated rotor head (b) and the complete configurations (c)

In a second step, the assembly (i.e. the Chimera blanking) between the near-body grids defining the different component and the off-body Cartesian mesh is performed. Two approaches are considered here, whether bodies are in relative motion or not, in the same way as it was achieved in [10]. In the case of moving bodies, the hole-cutting by moving bodies is performed within the *elsA* solver [13] at each time step, whereas hole-cutting by fixed bodies is achieved in a pre-processing stage, using Connector module [14].

In both cases, blanking is performed using reference surfaces by the X-Ray hole-cutting technique of Meakin [15]. Into the solver, these surfaces are the wall boundaries of moving grids, whereas they can be either the closed wall surfaces or their extension to remove Chimera interpolations out of the boundary layer. Figure 5 displays the result of blanking of different elements of the rotor head with each other body and background grids. The donor grids for interpolation are determined by bounding box intersection of the receiver grid attached to one component with the grids attached to the other components.

Off-body adaptive Cartesian mesh generation and Chimera assembly are performed in a pre-processing stage, using Cassiopée python modules [16]. CFD data (mesh, boundary conditions, connectivity, hole-cutting information) are stored in a CGNS/Python tree.

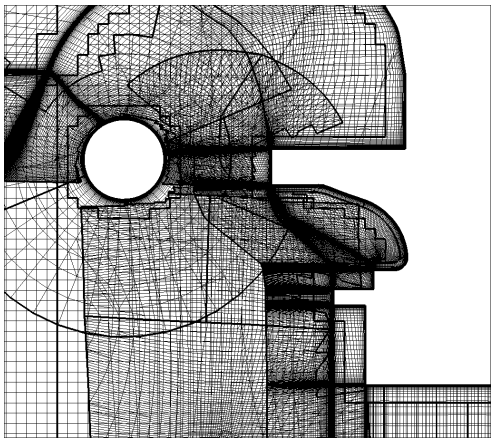

Figure 5 - Blanking of multiple elements of the rotor head

3. ISOLATED FUSELAGE

First application of the numerical methodology described above is the case of the isolated fuselage for a cruise flight condition. An angle of attack of -2° is considered as well as a cruise speed of 70 m/s. No steady solution could be obtained for this flow condition and a time-accurate simulation is performed. Time integration is ensured by a 2nd order Backward Euler scheme iteratively solved using the Gear method and 4 sub-iterations. The choice of the time step is based on the expected approximate vortex shedding frequency downstream the fuselage backdoor. Considering a Strouhal number of 0.2 based on freestream velocity and fuselage backdoor width, an approximate shedding period is defined and one percent of this period is taken as the time step in the simulation. A strong separation is indeed observed in the computational results as illustrated in Figure 6.

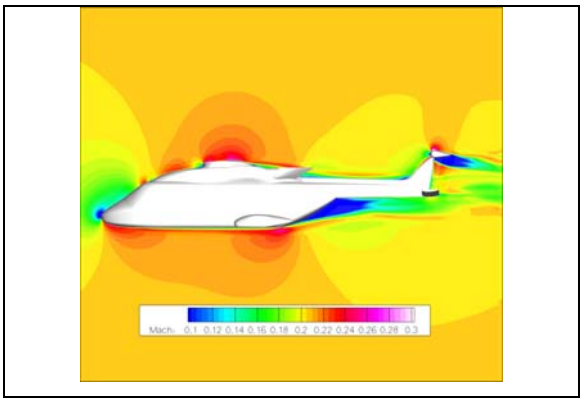

Figure 6 - Isolated fuselage computation - Mach number contours in the symmetry plane

The entire backdoor region is separated and the flow reattaches at the middle length of the tail-boom. This large separation produces a high pressure drag that corresponds to 68% of the total drag of the fuselage. The correct prediction of the backdoor separation is thus of primary importance for the total drag prediction. A detailed analysis of the flow shows that parts of the vortical structures are quickly dissipated when the off-body mesh coarsens (Figure 8, top). The fuselage wake capture is thus highly affected by the grid resolution downstream the fuselage, with probable consequence on the pressure drag. Feature-based adaptation of octree-based Cartesian grids is therefore performed, as detailed in [12] to improve the fuselage wake capture and the pressure drag prediction. The sensor used for adaptation is the Q-criterion, which highlights the flow regions where the rotational part of the flow dominates the sheared regions. Adaptation of the octree is performed with respect to the sensor. Threshold value of the Q criterion above which the octree is refined is automatically determined by controlling the number of points, which must be increased of 50% after adaptation. Furthermore, no additional refinement level is added during this step. A new set of Cartesian grids is generated according to this adapted octree. The resulting adapted off-body mesh is presented in Figure 7, showing an increased mesh density downstream the fuselage as expected. The final off-body Cartesian mesh after adaptation is made of 40 million points (fuselage grids: 7.8 Mpts, adapted off-body grids: 35.4Mpts). Figure 8 compares the Q-criterion iso-surfaces before and after off-body mesh adaptation. The capture of the fuselage wake is highly improved by the adaptation; the refined Cartesian mesh downstream the fuselage enables to decrease the numerical dissipation and allows the extension of the wake capture to a distance of more than one fuselage length downstream the fuselage fin.

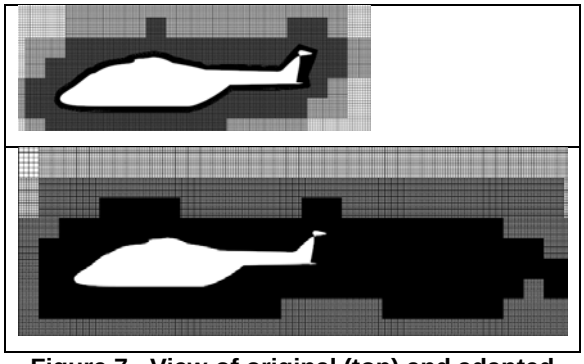

Figure 7 - View of original (top) and adapted (bottom) off-body Cartesian mesh

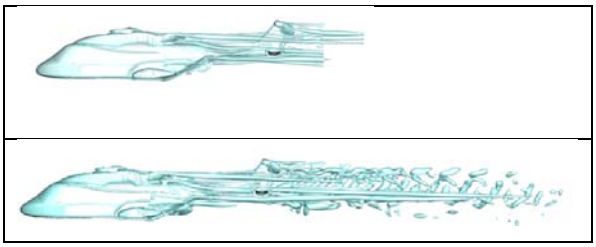

Figure 8 - Q-criterion iso-surface for the original (top) and adapted (bottom) off-body mesh

Table 2 compares the fuselage drag without and with off-body mesh adaptation as well as the drag decomposition into pressure drag and viscous drag (or friction drag). An increase of 5% of the total drag is observed after off-body mesh adaptation. Adaptation has no influence on the viscous drag, the total drag increase is only due to the increase of the pressure drag linked with the better capture of the fuselage wake. A correct capture of the fuselage wake is thus mandatory to have a correct prediction of the fuselage drag. Further analysis on the drag decomposition and drag sources could be done using the Far-Field Drag analysis as proposed and applied on aircraft configurations by Destarac [17].

Table 2 - Fuselage drag comparisons for original and adapted off-body meshes (non-dimensionalized by reference total drag)

	Original off-body mesh	Adapted off-body mesh
Total drag	1	1.05
Pressure drag	0.677	0.728
Viscous drag	0.323	0.322

Another interesting drag breakdown analysis is the decomposition of drag per fuselage elements as presented in Figure 9. It shows that the fuselage cabin (which is the centre part of the fuselage) is the main contributor of the drag production. This is in good agreement with the previous observation that pressure drag caused by the fuselage backdoor is predominant in the drag production.

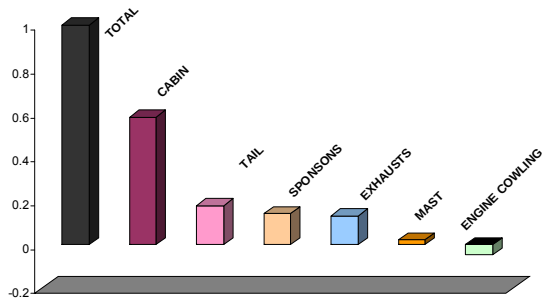

Figure 9 - Fuselage drag breakdown

Table 2 also shows that viscous drag accounts for 32% of the fuselage drag. It was demonstrated in [18] for example, that viscous drag prediction can be affected by laminar-turbulent transition for some fuselage geometry (2-5% of total drag). An evaluation of the laminarity effect for the present fuselage has thus been done. The 2-transport equations γ-Re_θ model proposed by Menter and Langtry [19] has been implemented in the *elsA* solver and is applied here. The original off-body mesh is used and the reference computation is run using the original Menter k-ω turbulence model. Comparison of this reference result and the one obtained by using in addition the γ-Re_θ model shows a very limited influence of the laminar-turbulent transition for this fuselage. Indeed, taking into account the transition leads to a difference of approximately 1% of the viscous drag. Figure 10 illustrates the result obtained with the transition prediction model and highlights the predicted laminar region on the fuselage. Only limited laminar region are predicted at the fuselage nose, the fin leading edge, and small areas on the sponsons and the horizontal stabilizer. This result shows that the fully-turbulent assumption can be done for the drag prediction on this particular fuselage.

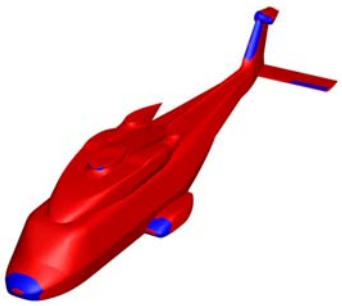

Figure 10 - Laminar region (blue) computed using the Langtry-Menter 2-transport equations for the transition prediction

4. ISOLATED ROTOR HEAD

The flow conditions are the same as previously for the isolated rotor head computations. The main rotor shaft is equal to -5° with respect to the fuselage, so the incidence angle is -7° in the rotor head reference frame. For unsteady computations, only the rotor rotation speed (Ω=995rpm) is taken into account, corresponding to an advance ratio $\mu=V/\Omega R=0.32$.

Solutions of a steady computation (15000 iterations) and of an unsteady computation (8 rotor revolutions) are compared. For the steady simulation, the four blades are located respectively at 45°, 135°, 225° and 315°. In terms of drag analysis, this position is supposed to be more representative of the unsteady configuration, according to literature.

Figure 11 presents the solution in the median place (Y=0) for both steady and unsteady simulations. The flow fields are quite different, as the global wake of the rotor head is convected lower in the steady configuration. When the rotor spins, the interaction of the other blade parts (stubs, attachments) can be detected upstream and downstream as seen in Figure 11 (right). Figure 12 shows also the differences with the representation of the wakes by an isosurface of the Q criterion. On the left-hand side (steady computation), the solution is quite symmetric with vortices emitted from the tip of the blade stubs. The rotor mast generates also a very “turbulent” wake. With the rotation, the wake of the front right blade is no more directly convected downstream but is emitted from the trailing edge and interacts with the rotor mast. A non-symmetric separation appears on the upper surface of the hub cap.

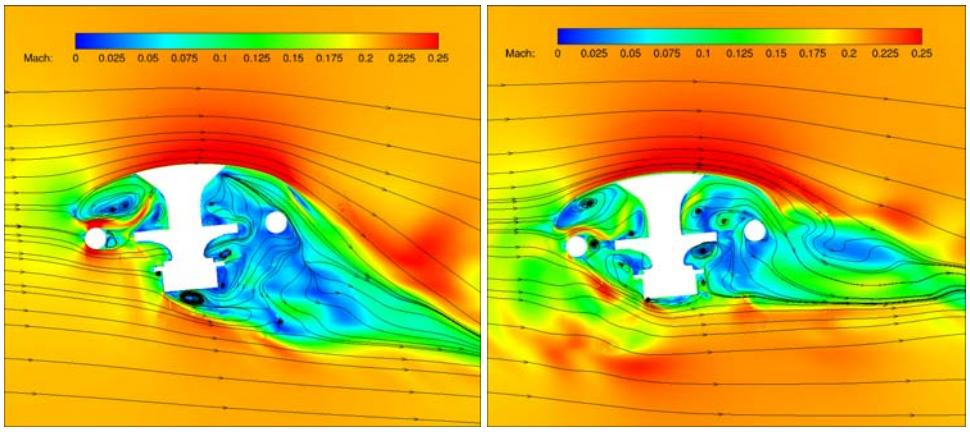

Figure 11 - Flowfield around the isolated rotor head for steady (left) and unsteady (right) computations

Figure 12 - Isosurface of Q criterion for steady (left) and unsteady (right) computations

Figure 13 presents the drag breakdown of the rotor head with the comparison of both steady and unsteady simulations. The most significant contribution to the global drag comes from the stubs, then the rotor mast and the blade attachments. The contribution of the pitch rods and the dampers to the drag is estimated to 4% each. The difference between the steady and the

unsteady results is weak in terms of percentages of the global drag: the contribution of the attachments to the drag is slightly increased. It can be due to stronger interactions with the stubs wake in the unsteady simulation. Figure 14 brings another indication on the difference between both calculations. Indeed, for the steady computation, the drag force converges to an averaged value with small fluctuations: only the rotor mast leads to vortex shedding, leading to oscillating drag force, even in steady mode. In the time-consistent simulation, the oscillations of the force are larger, even if the mean values are comparable with the steady computation (for example, the blade attachments contribution). In this second figure, it can be noticed that the drag contributions of the rotor mast and the blade stubs are decreased for the unsteady configuration, whereas the mean values for rods, dampers and attachments are not modified. Finally, the global drag of the rotating rotor head is decreased by 11% with respect to the steady computation.

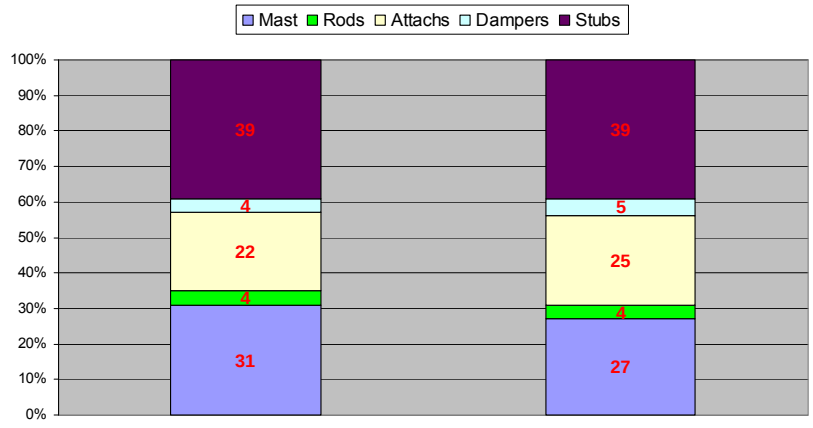

Figure 13 - Drag breakdown of the steady (left) and unsteady (right) isolated rotor head

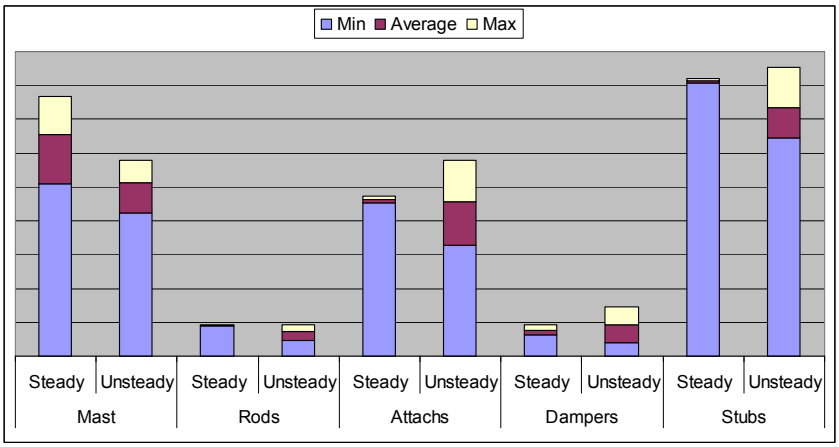

Figure 14 - Comparison of steady and unsteady configurations on drag contribution of each component

5. COMPLETE HELICOPTER

The complete configuration consists of the helicopter fuselage with the simplified rotor head. As their drag contribution is less than 4% of the global drag, the pitch rods have been removed to simplify the mesh generation. A steady computation has been first performed and is used as the initial condition to the unsteady simulation. Also, for steady mode, two blade positions have been evaluated: [0°, 90°, 180°, 270°] and [45°, 135°, 225°, 315°]. The values of the complete unsteady configuration have been chosen as reference in further drag analysis.

Figure 15 shows the flow field around the complete configuration: isocontours of Mach number and streamlines are plotted in the median plane (slice Y=0). In steady mode, when the blade

stubs are aligned with the fuselage, a massive separation appears aft of the rotor head until the vertical tail. For the [45°, 135°, 225°, 315°] stubs location, the flow reattaches the fuselage just behind the rotor head and the interaction with the vertical tail is less significant. Figure 15c displays an instantaneous view of the unsteady flow field. An instability appears between the rotor head and the rear parts of the helicopter, due to the wake of the rotating hub. This instability can be seen also in Figure 15 with the representation of the wake by an isosurface of the Q criterion. As described before, the interactions between the blade stubs and the hub cap or the upper parts of the fuselage seem to be stronger in the unsteady simulation.

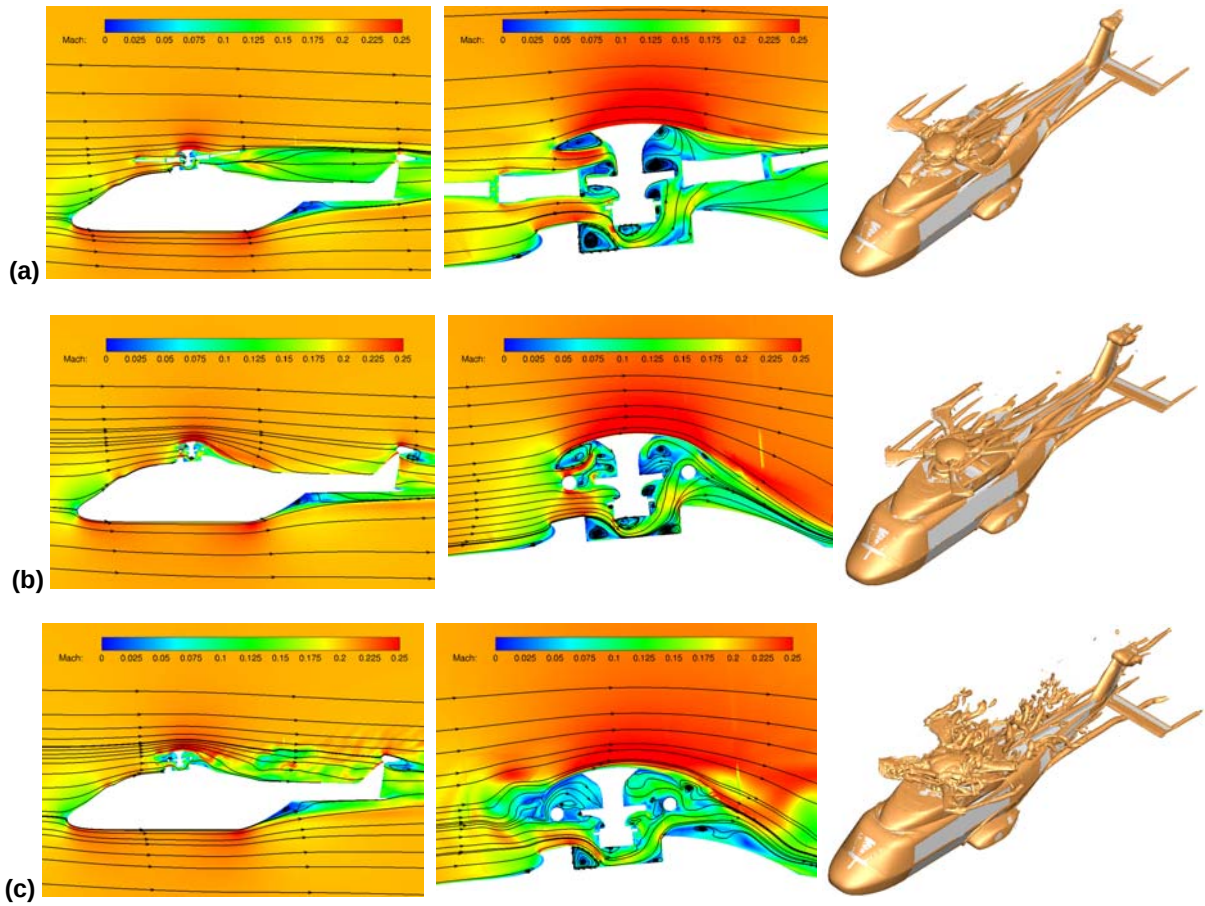

Figure 15 - Flowfield at slice Y=0 of the complete helicopter configuration and isosurface of Q criterion: (a) steady computation with blades at [0°, 90°, 180°, 270°], (b) steady computation with blades at [45°, 135°, 225°, 315°] and (c) unsteady computation

Figure 16 compares the drag contribution of the fuselage and the rotor head in three simulations of the complete configuration: a steady computation with blade stubs at [0°, 90°, 180°, 270°], a steady one with blade stubs at [45°, 135°, 225°, 315°] and an unsteady calculation. In this last computation, the drag coefficient of the complete helicopter is used as reference in the presented charts. Both steady simulations overestimate the drag by about 14%. The steady results with blade stubs at [45°, 135°, 225°, 315°] are in better agreement with the unsteady computation, as well as for the drag contribution of the rotor head. It represents 40% of the global drag for the "steady 0°" solution, 36% for the "steady 45°" solution and 32% for the unsteady simulation. The position of the blades has a negligible effect on the fuselage drag. The time consistency of the simulation has also a more significant effect on the rotor head drag than on the fuselage drag.

Figure 17 compares the drag coefficient of isolated fuselage and rotor head against the drag of these components, as part of the complete helicopter configuration. For the complete helicopter and the isolated rotor head, the results of the unsteady simulations have been taken into

account. The effect of the rotor head on the fuselage leads to increase the drag contribution of the fuselage by 19%. The effect of the fuselage on the rotor head tends to decrease the drag contribution of the rotor head (respectively by 7% and 15% for the steady and unsteady computations).

In perspective of the rotor head drag optimization, the simulation of the steady isolated rotor head will give a drag contribution overestimated by 24% with respect to its drag contribution of the unsteady complete helicopter configuration. This level of difference is quite important and cannot be taken as a reliable error: it includes too many parameters (steady/unsteady, isolated/complete configuration). On the other hand, in an optimization computational loop, unsteady complete configurations have to be avoided because of an important CPU time consumption.

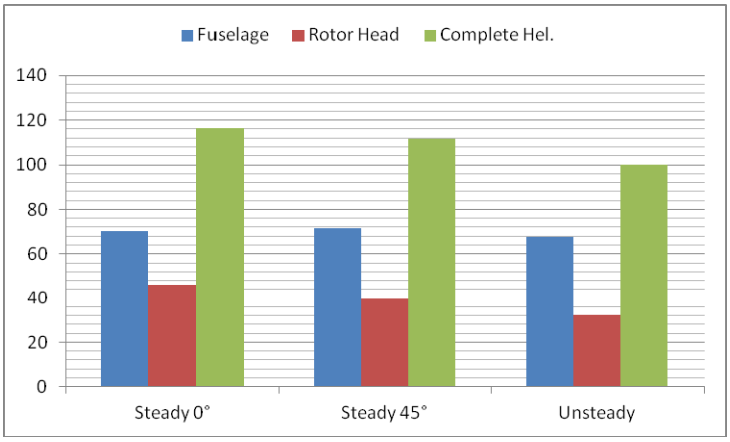

Figure 16 - Comparison of drag contribution (in %) in the complete configuration simulations

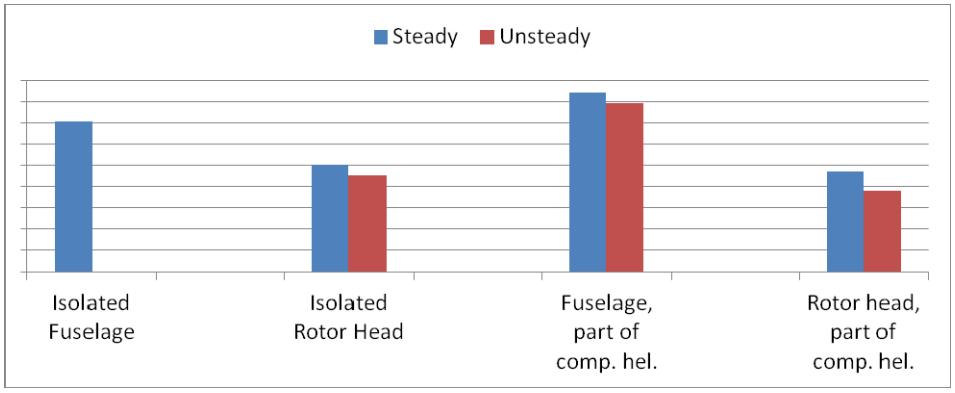

Figure 17 - Comparison of drag coefficient for isolated and complete configurations

6. CONCLUSION

This work concerns the drag prediction of the fuselage and its main rotor head by CFD using *elsA* structured solver. In order to deal with such a complex configuration and to analyze the influence of each geometrical component to the drag, we have chosen to partition the computational domain into near-body curvilinear grids and off-body adaptive Cartesian grids that are automatically generated. This simplifies the mesh generation process, since each geometrical component is meshed separately with a short extension into the domain. Cartesian grid resolution is adapted locally to the resolution of the near-body grids around the different components, despite the scale discrepancies. Near-body meshes around all the components and off-body Cartesian grids describe an overset grid system. Chimera assembly is then performed automatically to blank out cells lying inside bodies. Both off-body mesh generation and Chimera assembly are performed outside the solver, in a pre-processing stage, using Cassiopée modules. This approach is very promising for further optimization tasks, since it is important to have an automatic process to add and remove

components of the geometry.

This approach has been applied on different configurations, such as the isolated fuselage, the isolated rotor head and the complete helicopter. The results presented here have been focused on the drag breakdown of the different parts of the rotorcraft. The main conclusions are:

- For isolated fuselage drag, a good capture of the backdoor separation and the wake is mandatory for an accurate drag prediction. The laminar-turbulent transition has a negligible influence on fuselage drag and a fully-turbulent hypothesis can be done in the simulations.
- The main drag contribution of the rotor head comes from the blade stubs, the rotor mast with its cap and then the blade attachments. The drag coming from the pitch rods and the dampers is negligible.
- A steady computation is not fully representative of the unsteady wake around the rotor head or a complete helicopter. The drag is overestimated by 12% with non-rotating rotor. However, it is better to place the blades at [45°, 135°, 225°, 315°] in the steady simulation.
- In perspective of the rotor hub optimisation, the influence of other components and their interactions (blade stubs and attachments, fuselage) are significant.

7. ACKNOWLEDGEMENT

The present work has been partially funded by the European Union in the framework of the CleanSky Green Rotorcraft project.

8. REFERENCES

[1] T. W. Sheehy, D.R Clark, *A method for predicting helicopter hub drag*, United Technologies Corporation Report Nr. AD-A021 201, 1976.

[2] D. R. Graham, D. Y. Sung, L. A. Young, A.W. Louie, R.H. Stroub, *Helicopter Hub Fairing and Pylon Interference Drag*, NASA Technical Memorandum 101052, 1989.

[3] F. F. Felker, *An Experimental Investigation of Hub Drag on the XH-59A*, Paper Number AIAA-85-4065, AIAA 3rd Applied Aerodynamics Conference, Colorado Springs, 1985.

[4] S. Borie, J. Mosca, L. Sudre, C. Benoit, S. Péron, *Influence of rotor wakes on helicopter aerodynamic behaviour*, 35th European Rotorcraft Forum, Hamburg, 2009.

[5] F. Le Chuiton, T. Kneisch, S. Schneider, Ph. Krämer*, Industrial validation of numerical aerodynamics about rotor heads: towards a design optimisation at Eurocopter*, 35th European Rotorcraft Forum, Hamburg, 2009.

[6] J. O. Bridgeman, G.T. Lancaster, *Predicting hub drag on realistic geometries*, American Helicopter Society Aeromechanics Specialists' Conference, San Francisco, 2010.

[7] M. Dombroski, T.A. Legolf, *Drag Prediction of Two Production Rotor Hub Geometries*, 68th Annual Forum of the American Helicopter Society, Fort Worth, 2012.

[8] L. Cambier, S. Heib, S. Plot, *The ONERA elsA CFD software: input from research and feedback from industry*, 28th Congress of the International Council on the Aeronautical Sciences, Brisbane, 2012.

[9] T. Schwarz, *The GOAHEAD project, overview and selected results*, 36th European Rotorcraft Forum, Paris, 2010.

[10] T. Renaud, M. Costes, S. Péron, *Computation of GOAHEAD configuration with Chimera assembly*, Aerospace Science and Technology Journal, vol. 19(1), pp. 50–57, 2012.

[11] R. L. Meakin, *An efficient means of adaptive refinement within systems of overset grids*, AIAA paper 95-1722-CP, 1995.

[12] S. Péron, C. Benoit, *Automatic off-body overset adaptive Cartesian mesh method based on an octree approach*, AIAA paper 2011-3050, 2011.

[13] C. Benoit, G. Jeanfaivre, E. Canonne, *Synthesis of ONERA Chimera method developed in the frame of CHANCE programme*, 31st European Rotorcraft Forum, Florence, 2005.

[14] S. Péron, C. Benoit, *A python pre-processing module for Chimera assembly*, 10th Overset Grid Symposium, 2010.

[15] R. L. Meakin, *Object X-Rays for Cutting Holes in Composite Overset Structured Grids*, AIAA Paper 2001-2537, 2001.

[16] elsa.onera.fr/Cassiopee/Userguide.html

[17] D. Destarac, *CFD-based aircraft drag prediction and reduction*, von Karman Lecture Series, Hampton, 2013.

[18] HELIFUSE-Helicopter Fuselage Drag, Assessment report, Task 2 – *Navier-Stokes Calculations, Assessment of Blind Test Calculations*, Deliverable of subtask 2.1, HELIFUSE/C/1/DLR/03/1, 1997

[19] R. Langtry, F. Menter, *A Correlation-Based Transition Modeling for Unstructured Parallelized Computational Fluid Dynamics Codes*, AIAA Journal, Vol. 47, n°12, Dec2010, pp 2894-2906.